nature portfolio

https://doi.org/10.1038/s41929-021-00624-y

Supplementary information

Interplay of electrochemical and electrical effects induces structural transformations in electrocatalysts

In the format provided by the authors and unedited

Supplementary Information for

Interplay of electrochemical and electrical effects induces structural transformations in electrocatalysts

Feng Li[1,8], Xenia V. Medvedeva[1,8], Jury J. Medvedev[1], Evgeniia Khairullina[1,7], Helen Engelhardt[1], Skandan Chandrasekar[1], Yinzhou Guo[2], Jian Jin[3], Anna Lee[4], Héloïse Thérien-Aubin[2,5], Aftab Ahmed[6], Yuanjie Pang[3] and Anna Klinkova[1,*]

1. Department of Chemistry and Waterloo Institute for Nanotechnology, University of Waterloo, 200 University Ave W, Waterloo, Ontario N2L 3G1, Canada
2. Max Planck Institute for Polymer Research, Ackermannweg 10, 55128, Mainz, Germany
3. School of Optical and Electronic Information, Wuhan National Laboratory for Optoelectronics, Huazhong University of Science and Technology, 1037 Luoyu Road, Wuhan 430074, PR China
4. Department of Chemistry and Biochemistry, University of Minnesota Duluth, 1038 University Drive, Duluth, Minnesota 55812, United States
5. Department of Chemistry, Memorial University of Newfoundland, 283 Prince Philip Drive, Saint John's, Newfoundland A1B 3X7, Canada
6. Department of Electrical Engineering, California State University Long Beach, 1250 Bellflower Boulevard, Long Beach, California 90840, United States
7. Present address: Institute of Chemistry, Saint Petersburg State University, 26 Universitetskiy Prospect, Petergof, Saint Petersburg 199034, Russian Federation
8. These authors contributed equally.

*Correspondence to: aklinkova@uwaterloo.ca

This supporting information contains:

- Supplementary Notes 1-3
- Supplementary Methods
- Supplementary Tables 1-5
- Supplementary Figures 1-30
- Supplementary References

Supplementary Notes

Supplementary Note 1

Prior to the electrode preparation, freshly synthesized nanoparticles were washed to remove excess surfactant and other ionic species and concentrated for further use. The cathodes for electrochemical tests were prepared by depositing concentrated aqueous solutions of nanoparticles on Au (for Au BNPs and CCs) or Pd (for Pd BNPs and CCs) foils, followed by extensive washing with methanol to remove cationic surfactants from the surface of the particles[1]. Based on thermogravimetric (Supplementary Figure 22) and X-ray photoelectron spectroscopy (XPS) analyses (Supplementary Figure 23), the majority of the cationic surfactant were removed in this step, and any traces present were consistent across all metal nanoparticle samples to ensure comparable surface chemistry prior to starting the electrochemical tests. The cathodes were assembled in 0.5 M $KHCO_3$ electrolyte in a three-electrode electrochemical cell with Pt mesh and double junction saturated Ag/AgCl electrode used as counter and reference electrodes, respectively. Cyclic voltammetry (CV) in 0 to -0.6V vs RHE range under CO_2 atmosphere revealed that the electrochemical behaviour of the nanostructures remained stable after the initial activation of the surface in the first couple of sweeps (Supplementary Figures 24, 25). Based on the XPS analysis, cationic surfactant counterions present initially at the gold surface in trace amounts were removed during the first 3 CV cycles (Supplementary Figure 23a); Au existed in its metal state for both CCs and BNPs (Supplementary Figure 26a) and remained in that form after electrolysis (Supplementary Figure 23b).

Supplementary Note 2

Conceptually, EM is a migration process of metal atoms under applied current caused by the electron wind force, which is a transfer of momentum to the metal atoms from current carriers on their scattering. In the case of nonuniform current density distribution, EM can be described as a force driving atomic species from higher to lower current density regions to minimize current crowding. Generally, $J_{metal} \geq 10^4$ A/cm^2 are required to cause EM inside the metal, where it is significantly faster along the grain boundaries than in the bulk. At the same time, EM on surfaces and in thin films can be observed at ≥ 10 A/cm^2, as it is associated with the mobility of less coordinated surface atoms[2].

In addition, the nanostructure regions with high current density and, subsequently, high local power (Supplementary Figures 27, 28), can be subject to a local temperature increase by Joule heating, which can additionally promote the surface mass transport of the electrocatalyst material[3]. However, we found that the temperature increase via Joule heating was negligible in the systems studied in this work (Supplementary Figure 29), due to significant heat dissipation into the substrate metal film. We note that Joule heating may be more prominent and therefore should be evaluated in electrodes composed of nanoparticles with insulating surface modifiers or when substrates with low thermal conductivity are used.

Supplementary Note 3

The particle-particle and particle-substrate interfaces represent noticeable defects from a crystallographic perspective. While we employed nanoparticle synthesis methods that yield single crystalline nanoparticles[4], inevitable lattice discontinuities at their interfaces make these areas crystallographically similar to grain boundaries. In the case of CCs, the surfaces of synthesized particles are not perfectly flat, in contrast to the idealized FEM geometric models (Fig. 4c,h); thus, the imperfect contact at the particle-particle interface may result in even more pronounced current stressing than seen in Figure 4. In addition,

these NP surface imperfections may contain traces of adsorbates remaining from the synthesis, even though the majority of them was removed (Supplementary Fig. 22, 23a). Since the J_{metal} threshold for EM is a function of not only the metal nature and geometry, but also these nuances at the interfaces, it is difficult to be estimated quantitatively. However, it is reasonable to expect that Pd is more stable against EM than Au as the atomic mobility kinetics and thermodynamics simulations discussed in the DFT section generally show higher stability of Pd against surface mobility than Au (Fig. 3a).

Supplementary Methods

Materials. Gold foil (99.95%, thickness 0.05mm), palladium foil (99.9%, thickness 0.025mm), sodium salicylate (NaSal, 99%), BrijL23, and palladium(II) chloride ($PdCl_2$, 99.9%) were purchased from Alfa Aesar. Potassium bicarbonate ($KHCO_3$, 99.5-101.0%), hexadecyltrimethylammonium bromide (CTAB, ≥99.0%, BioUltra, for molecular biology), cetylpyridinium chloride monohydrate (CPC, UPS grade), L-Ascorbic acid (AA, ≥99%, anhydrous, ACS grade), gold(III) chloride trihydrate ($HAuCl_4x3H_2O$, ≥99.9%, used for the synthesis of Au BNPs), sodium borohydride ($NaBH_4$, ≥98.0%), copper(II) sulfate ($CuSO_4$, ≥99.99%), gold(III) chloride solution ($HAuCl_4$, 99.99%, 30 wt. % solution in dilute HCl), hydrogen peroxide (H_2O_2, 30 wt. % solution in H_2O), and sodium hydroxide (NaOH, ≥97%, ACS grade)were purchased from Sigma Aldrich. Hexadecyltrimethylammonium chloride (CTAC, >95.0%) was purchased from TCI America. Silver nitrate ($AgNO_3$, 99.98%) was purchased from Engelhard Industries. Toray carbon paper (060, Wet Proofed) was purchased from FuelCellStore.

All chemicals were used without further purification. All solutions were aqueous and freshly prepared before use. Ultrapure water (Millipore, 18.2 MΩ*cm) was used for all experiments.

Synthesis of Au-Au CCs. The synthesis of Au-Au CCs was previously reported by our group elsewhere[5]. Briefly, (i) 3 nm Au nanoparticles were synthesized by the addition of 0.6 mL of ice-cold 10mM $NaBH_4$ solution into the vigorously stirred mixture of 0.167 mL of 15mM $HAuCl_4$ and 10 ml of aqueous 0.1M CTAB. After two hours of aging, seed solution was diluted to 50 mL; 6 mL of this solution was added into the diluted to 1 L mixture of 100mL of 0.2M CTAB, 2.66 mL of 15mM $HAuCl_4$, and 50 mL of 0.12M AA under mild stirring. Resultant was left to react overnight undisturbed. As prepared Au octahedrons were concentrated to 5 mL, washed twice with water, and redispersed in 5 mL of water. (ii) Au@Ag CCs were synthesized by the consequent addition of 1 mL of 10mM $AgNO_3$ and 4 mL of 1M AA into the preheated to 60°C mixture of 2.5 mL of concentrated Au octahedrons and 5 mL of 0.3 M aqueous CPC solution. Reaction was left to proceed under intense stirring on the thermomixer for 1h, then cooled down, washed once, and redispersed in 62.5 mL of water. (iii) 0.1 mL of 1mM $HAuCl_4$ was added dropwise into 1 mL of the Au@Ag cubes at a rate of 2 mL/min under vigorous stirring on thermomixer, followed by the addition of 0.05 mL of H_2O_2. Resultant – Au-Au CCs – were washed once at a high speed, once at a low speed, concentrated, and used as prepared for the electrode preparation.

Synthesis of Au BNPs. Au BNPs were prepared according to the previously reported procedure[6]. Au seeds were synthesised by the addition of the 1 mL ice-cold 100mM $NaBH_4$ into the mixture of 1 mL of 10mM $HAuCl_4$, 1 mL of 10mM sodium citrate, and 36 mL of water under stirring. The resulting mixture was left undisturbed for 3 hours. Au BNP growth has been done in two steps. First, 0.1 mL of Au seeds were added to the aqueous mixture of 1 mL of 0.2M BrijL23, 1 mL of 0.1M CTAB, 0.08 mL of 10mM $HAuCl_4$, 0.01 mL of 5mM $AgNO_3$, 0.2 mL of NaSal, and 0.02 mL of 0.1M AA. Second, 0.1 mL of the solution that was prepared on the first step was added to the mixture of 10 mL of 0.2M BrijL23, 10 mL of 0.1M CTAB, 0.8 mL of 10mM $HAuCl_4$, 0.1 mL of 5mM $AgNO_3$, 2 mL of NaSal, and 0.2 mL of 0.1M AA. Resultant was vigorously shaken for 1 min, left undisturbed for 8 h, washed twice, concentrated, and then used for the electrode preparation.

Synthesis of small Au BNPs. Small Au BNPs were synthesised following the procedure for Au BNPs, but addition of NaSal was replaced by the addition of equimolar AA.

Synthesis of Au-Pd CCs and core-frames. Pd CCs were synthesised following a modified procedure described for the synthesis of Au CCs, where in step (iii) 0.1 mL of the 1mM Na_2PdCl_4 was used instead of $HAuCl_4$ and in step (ii) surfactant-rich solution was used to top up Ag cubes. Specifically, when 0.1M CTAC solution was used, a more closed cage structured was obtained (a) and when 0.1M CTAB solution was used more open frame-like cage structure was obtained (b).

Synthesis of Pd BNPs. The synthesis was performed according to the procedure reported elsewhere[7]. Firstly, Pd polygonal seeds were synthesised. 345 mg of CTAB was dissolved in 10 mL of 0.25mM solution of Na_2PdCl_4 in a 50 mL two-neck round-bottom flask, the solution was bubbled with Ar for 30 minutes under stirring at 30 °C, followed by the injection of 0.22 mL of 15mM ice-cold $NaBH_4$ aqueous solution. Then 0.168 mL of this solution was added to the mixture of 690 mg CTAB, 20 mL of 0.25mM Na_2PdCl_4, and 0.156 mL of 0.1M AA. Resultant was shaken for 1 minute and left undisturbed for 2 h. Secondly, seed-mediated growth of branched Pd nanoparticles was performed. 1g of CTAB was dissolved in 6.8 mL of water and stirred at 30 °C, then 1 mL of 100mM $CuSO_4$ was added, followed by the consequent addition of 3.2 mL of a solution containing 100mM of Na_2PdCl_4 and 0.25 M of HCl, and 10 mL of the polygonal seeds, and 5 mL of 1M AA. Resulting mixture was stirred for 24 hours at 45 °C, washed 2 times, concentrated, and then used for the electrode preparation.

Supplementary Tables

Supplementary Table 1. Nanoscale void-containing reduction CO_2RR electrocatalysts and their stability.

ID	Electrocatalyst composition	Size	Structure	Structure description	Test of stability	Ref.
a	**$CuSnO_2$**	26.5±3.5 nm	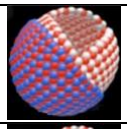	Hollow nanospheres	Stable current density and FEs of the products during **10h** electrolysis in CO_2-saturated 0.1M $KHCO_3$ at **-0.7V** vs RHE. No significant changes in the morphology of nanoparticles (TEM data) were observed.	[8]
b	**$CuSnO_2$**	32.5±4.5 nm	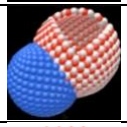	Cu NPs/Hollow SnO_2 Janus structures	Stable current density and FEs of the products during **10h** electrolysis in CO_2-saturated 0.1M $KHCO_3$ at **-0.7V** vs RHE. ***Changes in morphology have not been studied.***	[8]
c	**AuCu**	50-100 nm		Thin-walled hollow nanospheres	Current density and FE of the CO decreased slightly during **12h** electrolysis in CO_2-saturated 0.5M $KHCO_3$ at **-0.7V** vs RHE. No obvious changes in the morphology of nanoparticles (TEM data) were observed.	[9]
d	**Cu**	110±20 nm		Nanocavities	Current density and FEs of C_3-products significantly decreased after **2.5h** of electrolysis in a flow-cell configuration with GDE (1M KOH electrolyte) at **-0.56V** vs RHE. Catalyst reconstructed to form aggregated Cu nanoparticles (SEM data).	[10]
e	**Au**	120 nm		Concave rhombic dodecahedral nanoparticles	Current density was stable during **8.3h** electrolysis in CO_2-saturated 0.5M $KHCO_3$ (potential not specified). The concave features were maintained (SEM data).	[11]
f	**Cu**	≈ 700 nm	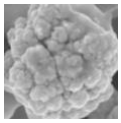	Porous microspheres	Current density increased without significant changes in average FE of C_2H_4 during **10h** electrolysis in CO_2-saturated 0.05M $KHCO_3$ + 0.05M KI at **-1.1V** vs RHE. No significant changes in the morphology of nanoparticles (SEM data) were observed.	[12]
g	**Au**	≈ 1µm	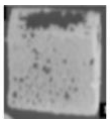	Hollow cubic NPs	Stability of the catalyst has not been studied.	[13]
h	**Cu_2O@Au**	≈ 1µm	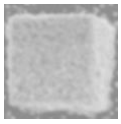	Hollow cubic nanocomposites	Stability of the catalyst has not been studied.	[13]
i	**Ag**	≈ 1.2 µm		Hollow porous microspheres	Current density was stable, and FE of CO slightly decreased after 10**h** of electrolysis in 0.1M $NaHCO_3$ at **-0.845V** vs RHE. No significant changes in the morphology of nanoparticles (SEM and TEM data) were observed.	[14]
j	**$(CoOH)_2CO_3$**	≈ 2 µm		Hollow urchin-like structures	Stable current density and FE of MeOH during **10h** electrolysis in CO_2-saturated 0.1M $NaHCO_3$ at **-0.25V** vs RHE. No significant changes in the morphology of nanoparticles (SEM and TEM data) were observed.	[15]

Supplementary Table 2. Nanoscale void-containing reduction HER electrocatalysts and their stability.

ID	Electrocatalyst composition	Size	Structure	Structure description	Test of stability	Ref.
a	**PtCu**	17.7 nm		Dodecahedral nanoframes	Little changes in polarization curves after **1000 CV** cycles. Current density decreased slightly after **2.8h** electrolysis in 0.5M H_2SO_4 at **-0.05V** vs RHE. No significant changes in the structure of nanoparticles, except the broken of some ultrathin edges (TEM data).	[16]
b	**PdPt**	17.5-21.5 nm		Bilayer nanocages with sub-nanometer thin shells	The mass activities of nanocages given as kinetic current densities at -0.05V vs RHE reduced by 24% after **10000 CV** cycles in 0.5M H_2SO_4. ***Changes in morphology have not been studied.***	[17]
c	**CuNi**	62 nm		Mesoporous nanocages	Little changes in polarization curves after **2000 CV** cycles. Current density decreased slightly during **8h** electrolysis in 1M KOH at **-0.022V** vs RHE. ***Changes in morphology have not been studied.***	[18]
d	**RuCoP**	200 nm		Ru NPs doped into CoP nanocage	Little changes in polarization curves after **1000 CV** cycles in 0.5M H_2SO_4. Initial current was decreased by 16% after continuous operation of **10h**. No significant changes in the morphology of nanoparticles (TEM data) were observed.	[19]
e	**CoFeSeP**	300 nm		Mesoporous nanostructured frames	No changes in polarization curves after **1000 CV** cycles in 0.5M H_2SO_4. Current density was relatively stable during **40h** electrolysis in 0.5M H_2SO_4 at constant overpotential of **0.07V** vs RHE. No significant changes in the morphology of nanoparticles (SEM data) were observed.	[20]
f	**CoSP**	450 nm		Yolk-shell microspheres	Current density was stable during **20h** electrolysis in 0.5M H_2SO_4 at constant overpotential of **0.135V** vs RHE. ***Changes in morphology have not been studied.***	[21]
g	**$NiCo_2S_4$**	550 nm		Double-shelled hollow nanospheres	Little changes in polarization curves after **2000 CV** cycles in 1M KOH. No significant changes in the morphology of nanoparticles (SEM and TEM data) were observed.	[22]
h	**$CoSe_2$/(NiCo) Se_2**	400-600 nm		Box-in-box hollow nanocubes	Little changes in polarization curves after **2000 CV** cycles in 1M $NaClO_4$. Small changes in the morphology of nanoparticles (SEM and TEM data) were observed.	[23]

Supplementary Table 3. Nanoscale void-containing reduction NRR and ORR electrocatalysts and their stability.

ID	Electrocatalyst composition	Size	Structure	Structure description	Test of stability	Ref.
Electrocatalysts for ***Nitrogen*** Reduction Reaction						
a	**Au**	35 nm	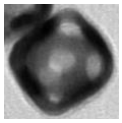	Nanocages	Current density was stable, and FE of the NH_3 decreased slightly during **12h** (5 runs) electrolysis in N_2-saturated 0.5M $LiClO_4$ at **-0.4V** vs RHE. At more negative than -0.6V potentials current density was not stable. ***Changes in morphology have not been studied.***	[24]
b	**Au-Ag_2O**	40 nm	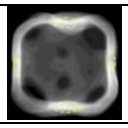	Bimetallic nanocages	Current density was relatively stable during **12h** electrolysis in N_2-saturated 0.5M $LiClO_4$ at **-0.3V** and -**0.4V** vs RHE, but not stable at **-0.5V**. ***Changes in morphology have not been studied.***	[25]
Electrocatalysts for ***Oxygen*** Reduction Reaction						
c	**$Pt_4PdCu_{0.4}$**	10 nm		Alloy nanoframes	Little changes in polarization curves after **2000 CV** cycles in 0.1M $HClO_4$. Nanoframes largely maintained original structures while a few nanoboxes have been slightly fractured after stability test (TEM data).	[26]
d	**Pt**	18nm		Cubic nanoframes	No significant aggregation after **30000 CV** cycles in O_2 sat. 0.1M $HClO_4$. Nanoframes slightly deformed, but their open structure was still retained (TEM data) after stability test. However, the cubic nanoframes shrank in terms of particle size and the average thickness of their ridges increased from 1.7 to 2.6 nm.	[27]
e	**$PtNi_3$**	20.1±1.9 nm		Nanoframes	Negligible changes in polarization curves after **10000 CV** cycles in 0.1M $HClO_4$. No significant changes in morphology of nanoparticles (bright- and dark-field STEM data) were observed.	[28]
f	**PtCu**	20 nm	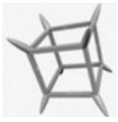	Octopod nanoframes	Small changes in polarization curves after **10000 CV** cycles in O_2 sat. 0.1M $HClO_4$. No significant changes in the morphology of nanoparticles (STEM and TEM data) were observed.	[29]
g	**PtCuPd**	20 nm	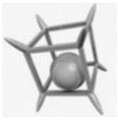	Yolk-shell octopod nanoframe	Significant changes in polarization curves after **10000 CV** cycles in O_2 sat. 0.1M $HClO_4$. ***Changes in morphology have not been studied.***	[29]
h	**CuPt**	30 nm		Rhombic dodecahedral nanoframes	A few segregated nanocrystals were observed (TEM data) after **1200 CV** cycles in O_2 sat. 0.1M $HClO_4$, but frame skeletons were still well-defined.	[30]
i	**CuPt**	30 nm		Spiny rhombic dodecahedral nanoframes	Nanoparticles distorted in their frame structure (TEM data) after **1200 CV** cycles in O_2 sat. 0.1M $HClO_4$, and the extended {100} vertices evolved rounded.	[30]
j	**PtCu**	40 nm	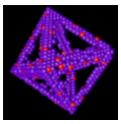	Spiny alloy octahedral nanoframes	Small changes in polarization curves after **8000 CV** cycles in O_2 sat. 0.1M $HClO_4$. The XPS characterization showed that the chemical state of PtCu structure did not change. No significant changes in the morphology of nanoparticles (TEM data) were observed.	[31]

Supplementary Table 4. Statistical analysis of nanoparticle sizes before and 5 hours of CO_2RR electrolysis obtained using Image-J software. On average, 100 nanoparticles were analyzed for each measurement.

Nanoparticle shape type	As-synthesized size, nm ± SD	Size after 5h CO_2RR, nm ± SD
Standard Au BNPs (overall diameter | arm length| arm width)	265±51 | 127±31 | 31±8	256±35 | 124±20 | 29±7
Small Au BNPs (overall diameter | arm length | arm width)	112±15 | 54±13 | 15±4	113±14 | 50±16 | 19±4
Au CCs (side length)	29±3	N/A***
Pd BNPs (overall diameter | arm length | arm width)	133±12 | 45±12 | 17±4	139±16 | 46±16 | 21±5****
Standard Pd CCs (side length)*	25±2	26±2****
Pd CCs – more open structure (side length)**	26±2	27±2****

*These measurements correspond to Pd CCs with a closed wall structure (see Extended Data Figure 2a-d).
** These measurements correspond to Pd CCs with an open wall structure (see Extended Data Figure 2e-h).
*** After 5 hours of CO_2RR electrolysis, no definitive side measurements could be obtained due to the disfigurement of Au CCs.
****A slight increase in the size of Pd nanoparticles after electrolysis in aqueous medium is related to Pd hydride formation and associated lattice expansion from 388.9 pm to 402.5 pm[32].

Supplementary Table 5. Surface roughness assessment of the fabricated Au electrodes.

Material	$Q_{Pb\ stripping}$ ($\mu C\ cm^{-2}$)	Roughness factor
Au (111)[33]	272	1
Au CCs	1479	5.44
Au BNPs	2453	9.02

Supplementary Figures

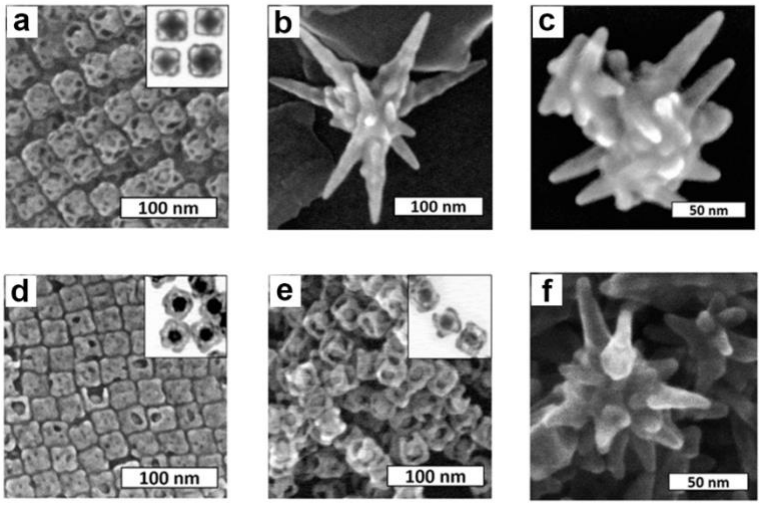

Supplementary Figure 1. Scanning electron microscopy (SEM) images of nanoparticles used in this work. (a) Au CCs with side length of 29±3 nm; (b) regular Au BNPs with arm length of 127±31 nm and arm width of 31±8 nm; (c) small BNPs with arm length of 54±13 nm and arm width of 15±4 nm; (d) regular Pd CC side length of 25±2 nm obtained using hexadecyltrimethylammonium chloride as a surfactant; (e) Pd CCs with more open structure and side length of 25±2 nm obtained using hexadecyltrimethylammonium bromide as a surfactant; (f) Pd BNPs with arm length of 82±21 nm and arm width of 19±4 nm.

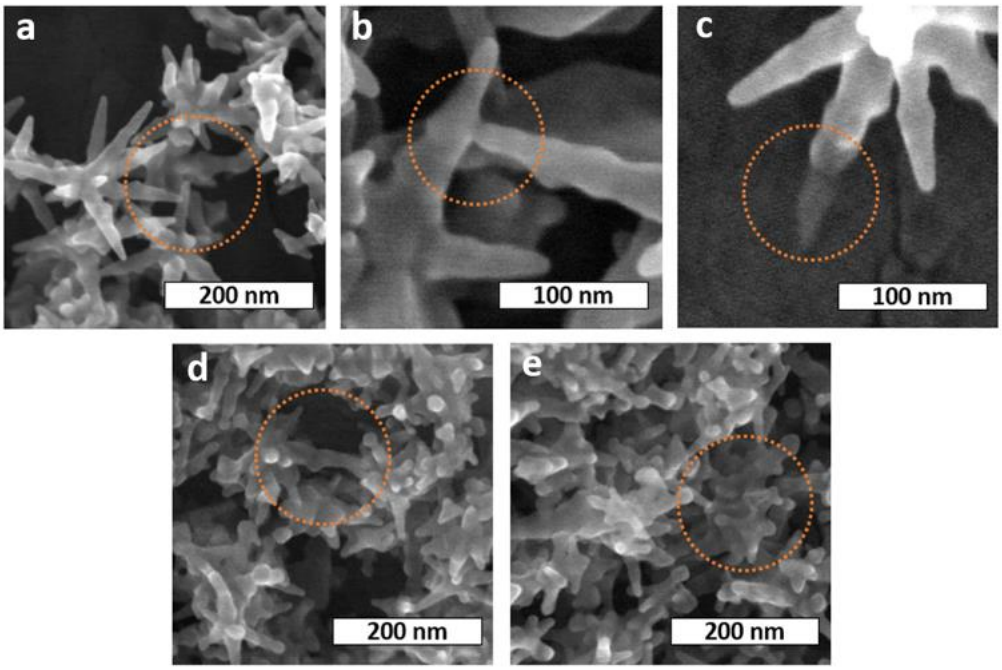

Supplementary Figure 2. Illustration of Au BNPs sintering. SEM images of standard Au BNPs sintering in a pile (a), sintering of tips (b), and sintering of a tip with Au substrate (c); and of small Au BNPs sintering of tips (d), and sintering in a pile (e) after 300 min of CO_2RR reaction at -0.6V vs RHE.

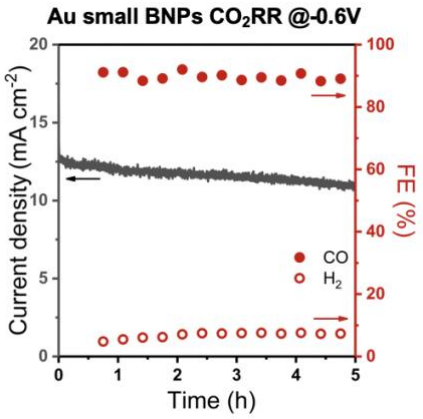

Supplementary Figure 3. CO_2 reduction activity of small Au BNPs over time during potentiostatic electrolysis at -0.6V vs RHE in CO_2-saturated 0.5M $KHCO_3$: changes in total current density (left axis) and Faradaic efficiencies (right axis) of CO (solid circles) and H_2 (empty circles) are shown as a function of time.

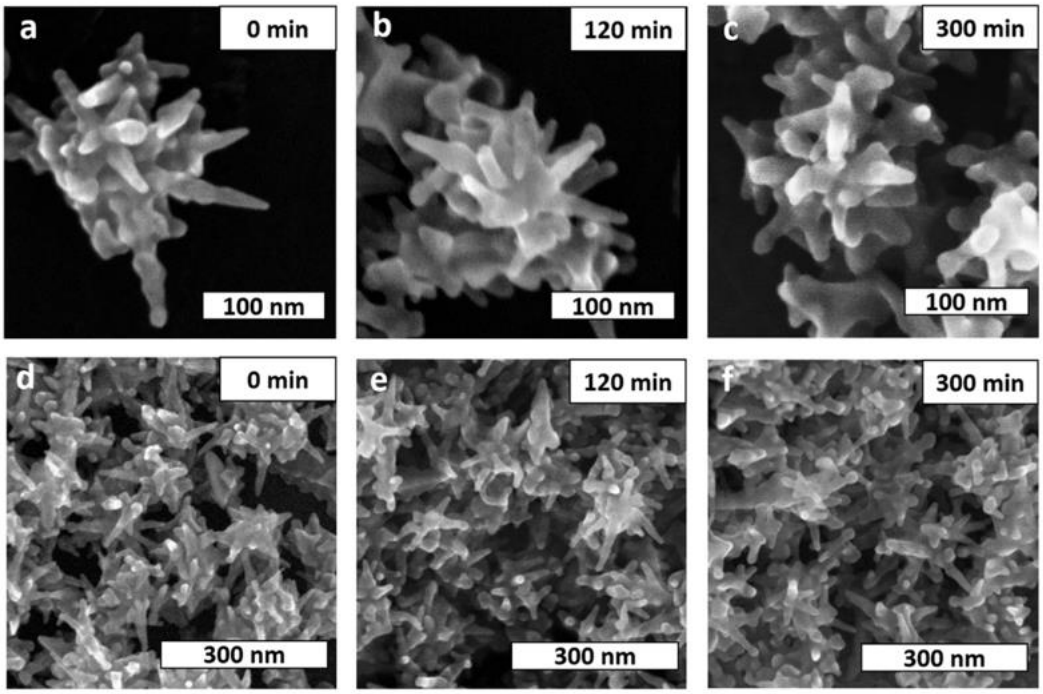

Supplementary Figure 4. SEM images of small branched Au nanoparticle before (a,d), after 120 min (b,e), and after 300 min (c,f) of CO_2RR reaction at -0.6V vs RHE at different magnifications.

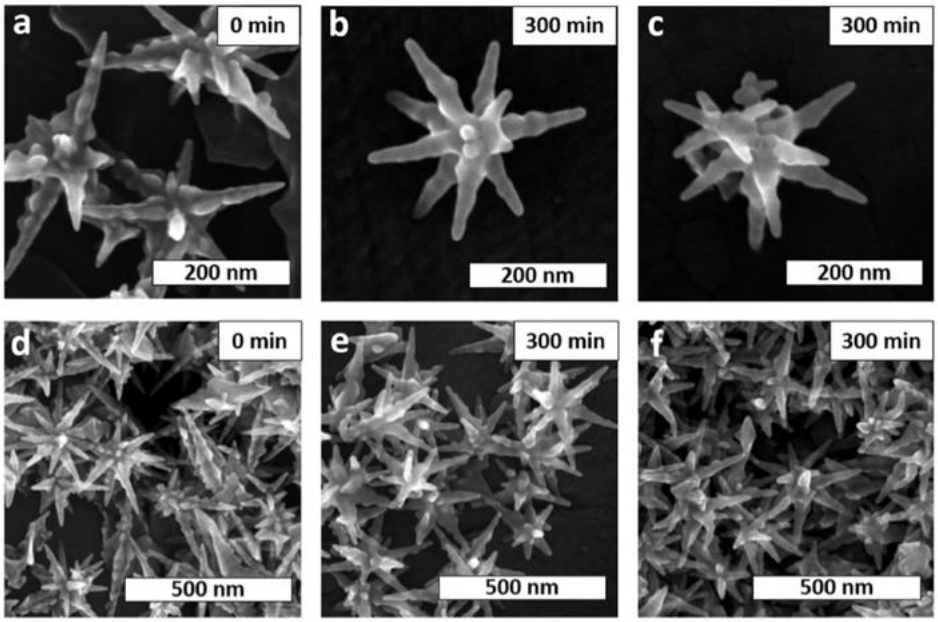

Supplementary Figure 5. Structural evolution of branched Au nanoparticles. SEM images of branched Au nanoparticles before (a,d) and after 300 min of CO_2RR reaction at -0.6V (b,e) and -1.2V (c,f) vs RHE at different magnifications.

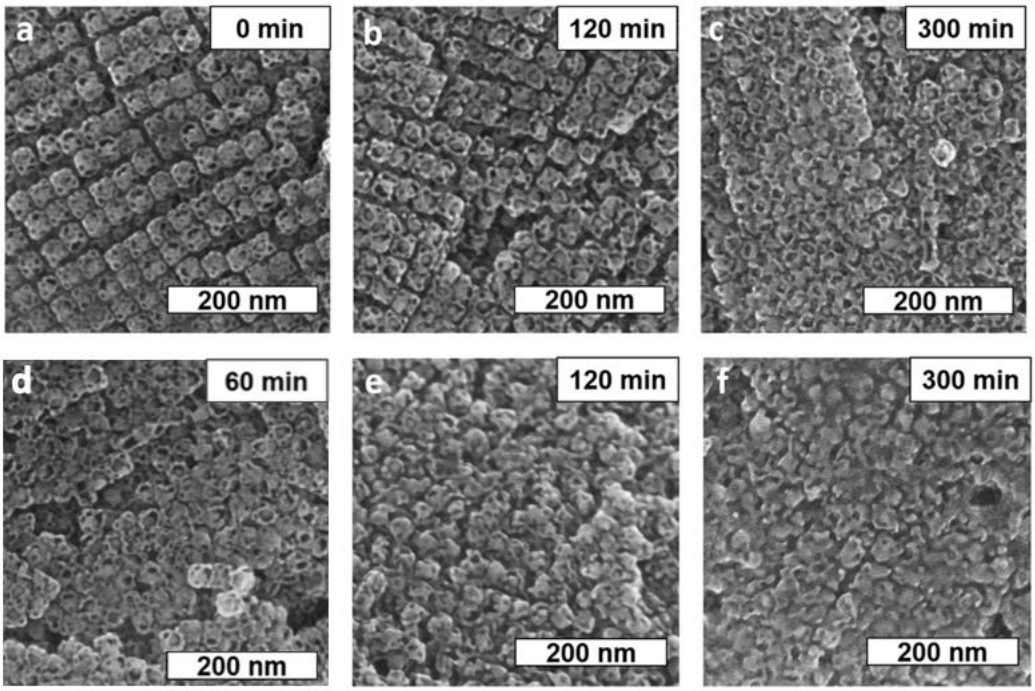

Supplementary Figure 6. SEM images of Au-Au CCs before (a), after 120 min (b), and 300 min (c) of HER at -0.6V vs RHE, and after 60 min (d), 120 min (e), and 300 min (f) of CO_2RR reaction at -0.6V vs RHE.

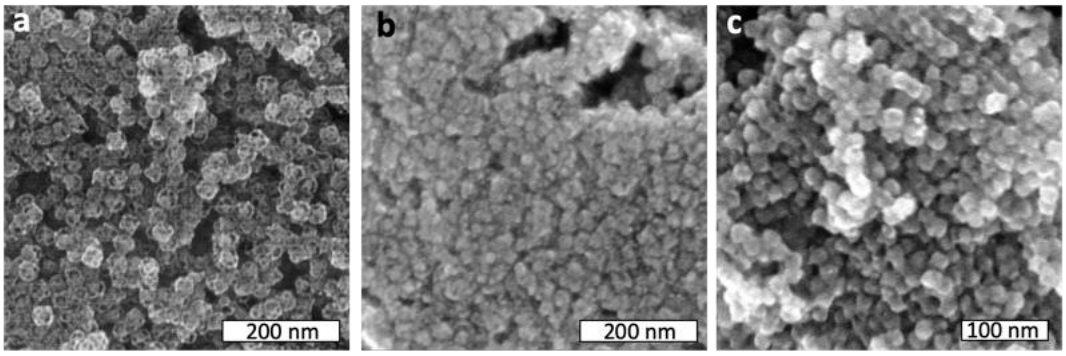

Supplementary Figure 7. (a,b) SEM images of Au CCs after 30 min (a) and 60 min (b) of CO_2RR at -1.2V vs RHE. (c) Disfigurement of Au CCs observed after potential overload error when running electrolysis at -0.6V vs RHE for 30 min.

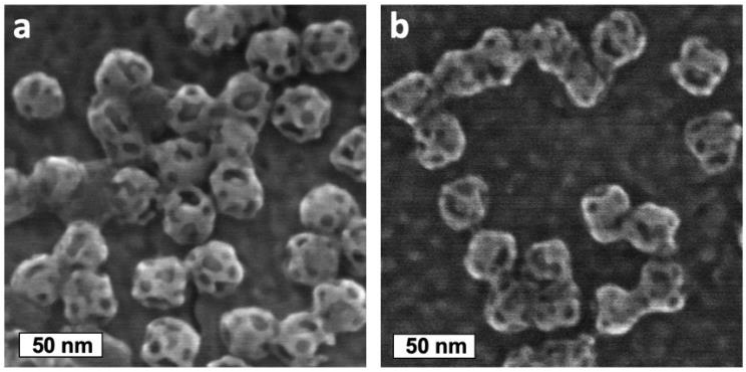

Supplementary Figure 8. (a,b) SEM images of Au CCs after 60 min of electrolysis under CO_2RR conditions in CO_2-saturated 0.5M $KHCO_3$ at -0.6V vs RHE. The loading of CCs in these experiments is twice lower than in the standard fully covered electrode samples.

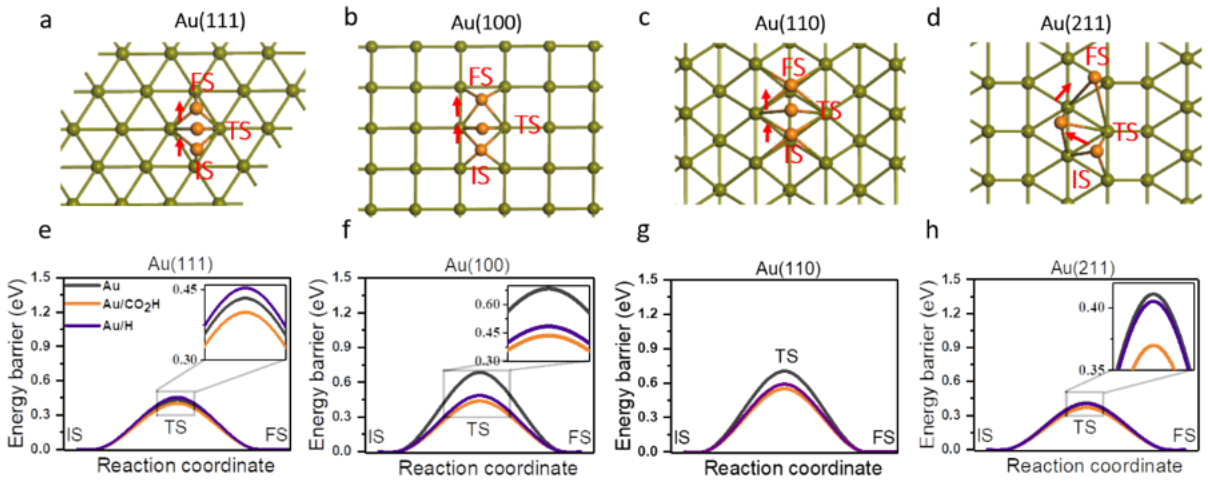

Supplementary Figure 9. Au atom mobility differentiation based on reaction intermediates present in the media. (a-d) the hooping paths studied for surface atom migration on Au(111), Au(100), Au(110) and Au(211) surfaces, with the olive colour atoms representing the Au surface and orange colour atoms representing the hooping Au atom and intermediate-bound Au atoms (Au-COOH and Au-H). (e-h) calculated energy barriers for migration path of Au atom, Au-COOH (CO_2RR) and Au-H (HER) intermediate-bound Au atoms on Au(111), Au(100), Au(110) and Au(211) surfaces, respectively.

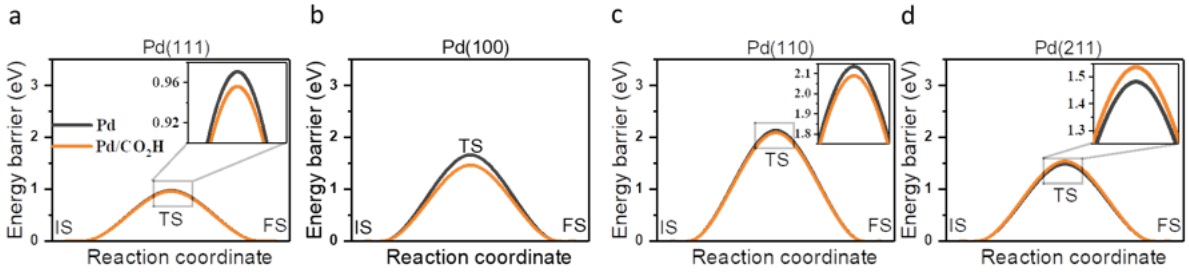

Supplementary Figure 10. Calculated energy barriers for migration path of Pd atom and Pd-COOH (CO_2RR) intermediate-bound Au atom, with (a-d) for Pd(111), Pd(100), Pd(110) and Pd(211) surfaces, respectively. The paths studied for Pd are the same as that for Au.

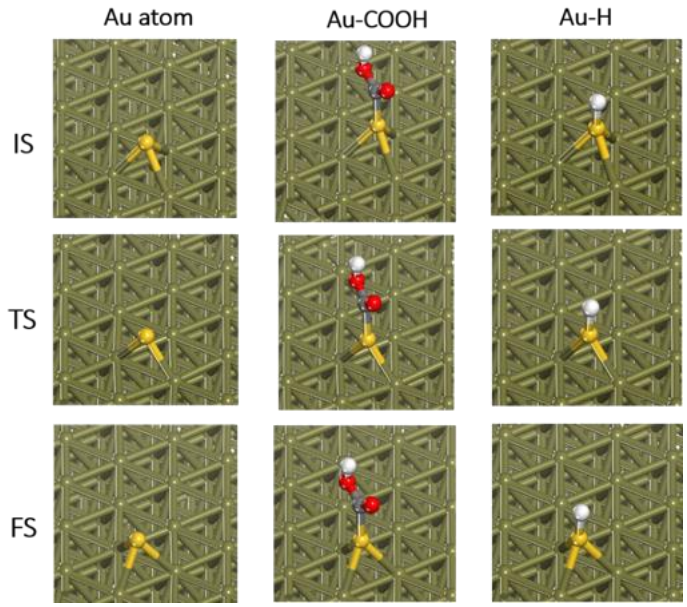

Supplementary Figure 11. Optimized geometry structures for initial, transition and final states of migration for Au atom and intermediate-bound Au atoms of Au-COOH(CO_2RR) and Au-H(HER) on Au(111) surface, respectively. The olive colour atoms represent Au substrate surfaces, with yellow, grey, red and white colour atoms representing hooping Au, C, O and H atoms respectively

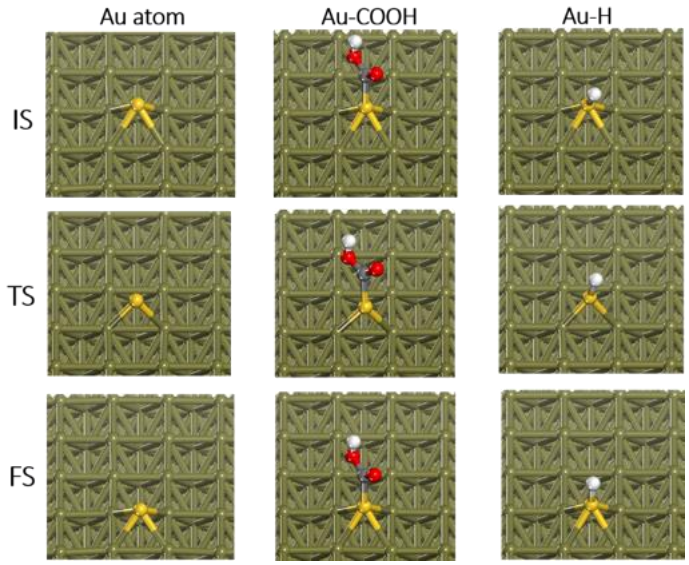

Supplementary Figure 12. Optimized geometry structures for initial, transition and final states of migration for Au atom and intermediate-bound Au atoms of Au-COOH(CO_2RR) and Au-H(HER) on Au(100) surface, respectively.

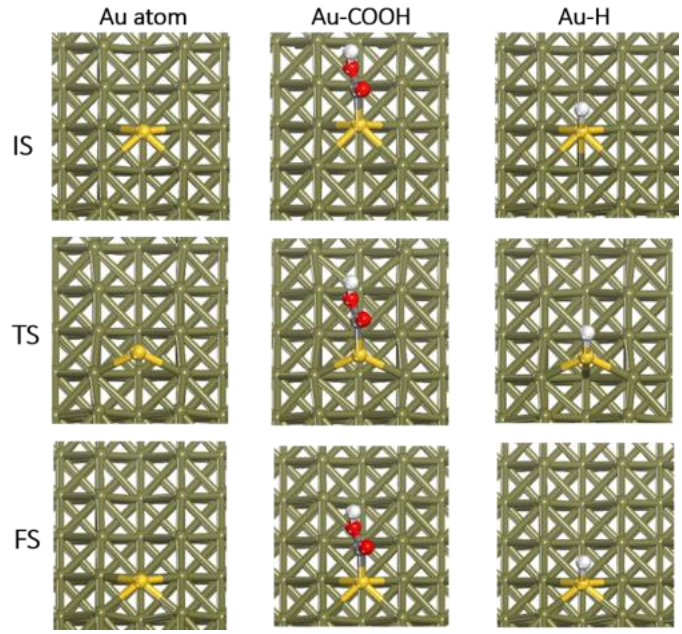

Supplementary Figure 13. Optimized geometry structures for initial, transition and final states of migration for Au atom and intermediate-bound Au atoms of Au-COOH(CO_2RR) and Au-H(HER) on Au(110) surface, respectively.

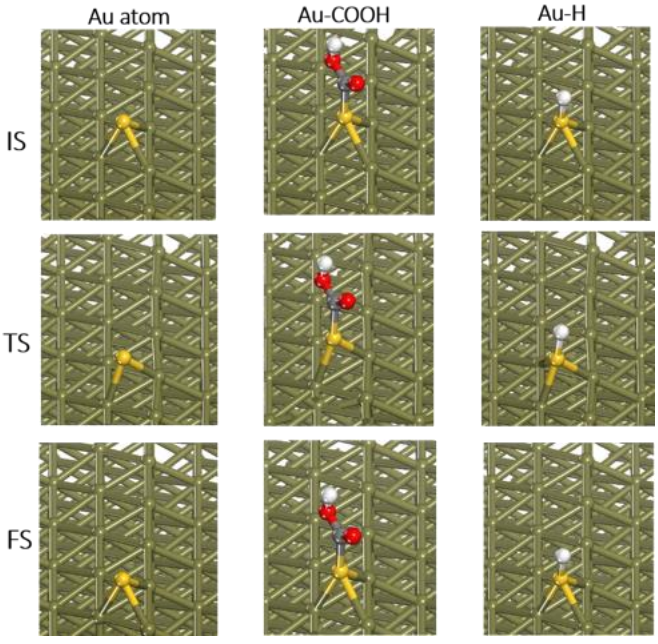

Supplementary Figure 14. Optimized geometry structures for initial, transition and final states of migration for Au atom and intermediate-bound Au atoms of Au-COOH(CO_2RR) and Au-H(HER) on Au(211) surface, respectively.

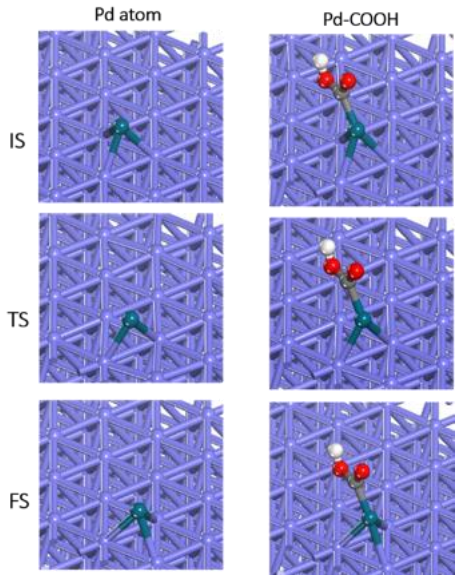

Supplementary Figure 15. Optimized geometry structures for initial, transition and final states of migration for Pd atom and intermediate-bound Pd atom of Pd-COOH(CO_2RR) on Pd(111) surface respectively. The lavender colour atoms represent Pd surfaces, with teal, grey, red and white colour atoms representing hooping Au, C, O and H atoms, respectively.

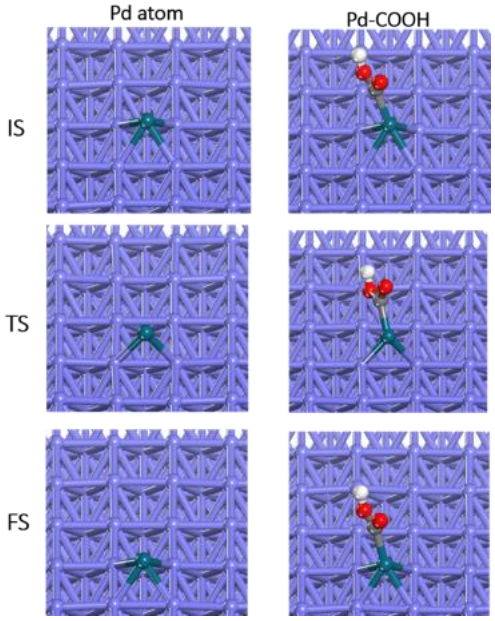

Supplementary Figure 16. Optimized geometry structures for initial, transition and final states of migration for Pd atom and intermediate-bound Pd atom of Pd-COOH(CO_2RR) on Pd(100) surface, respectively.

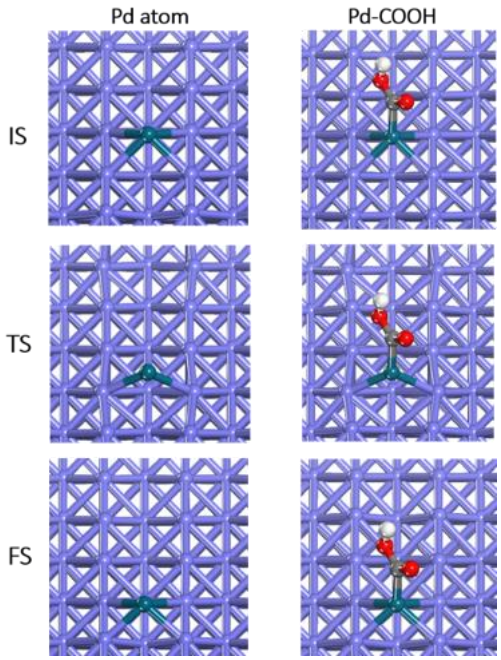

Supplementary Figure 17. Optimized geometry structures for initial, transition and final states of migration for Pd atom and intermediate-bound Pd atom of Pd-COOH(CO2RR) on Pd(110) surface, respectively.

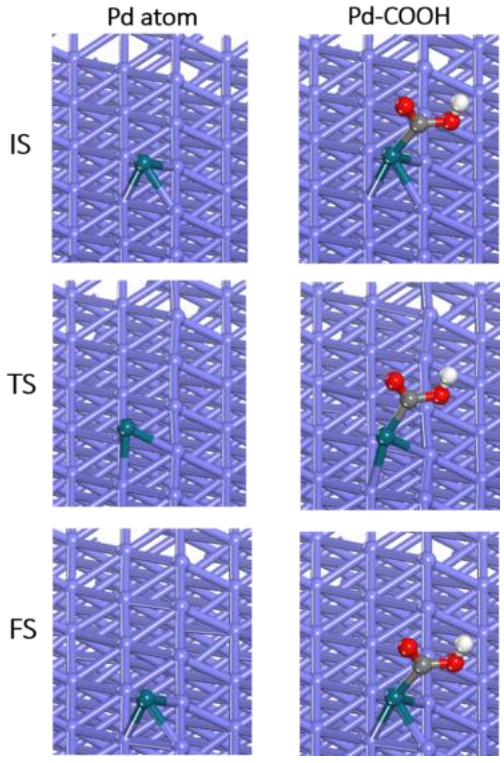

Supplementary Figure 18. Optimized geometry structures for initial, transition and final states of migration for Pd atom and intermediate-bound Pd atom of Pd-COOH(CO_2RR) on Pd(211) surface, respectively.

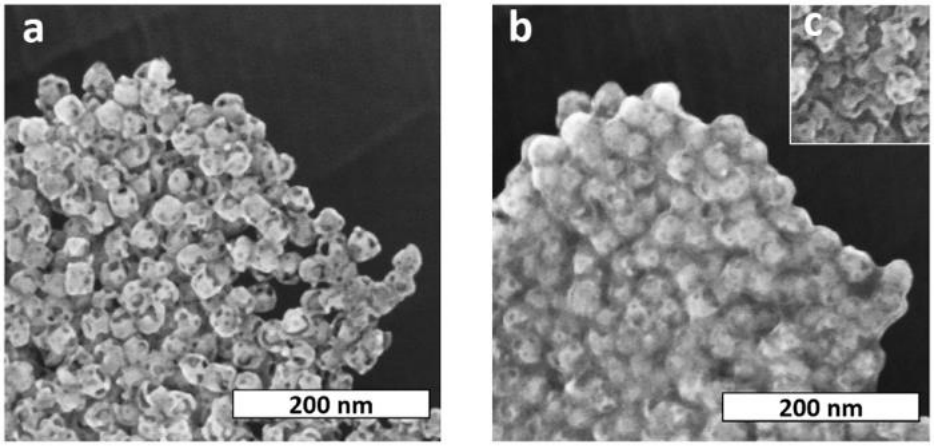

Supplementary Figure 19. Identical location SEM imaging attempt. (a, b) SEM images of the identical location on the same Au CC cathode after 30 min (a) and 60 min (b) of CO_2RR reaction at -0.6V vs RHE. Insert (c) shows an area of Au CC cathode after 60 min of CO_2RR at -0.6V vs RHE that was not previously affected by the electron beam. The observed contamination revealed that identical location imaging provides convoluted data, and a fresh area analysis must be performed to provide reliable information about the structural change of the particles.

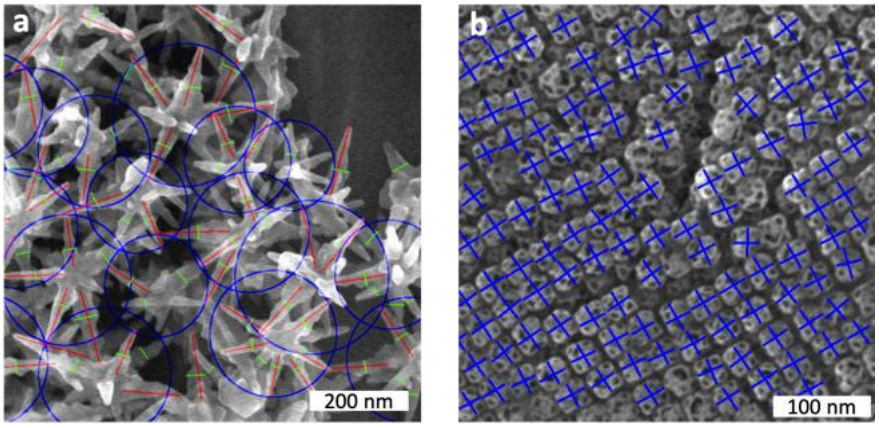

Supplementary Figure 20. Examples of statistical analysis of the size distribution in nanostructures using Image-J software. (a) The overall sizes of BNPs are marked with blue circles (the diameter of the circle corresponds to the average overall size), the arm lengths are marked with red lines, and the arm width measured in the middle of each arm is marked with green lines. (b) The CCs were characterised by the side length, marked with blue lines.

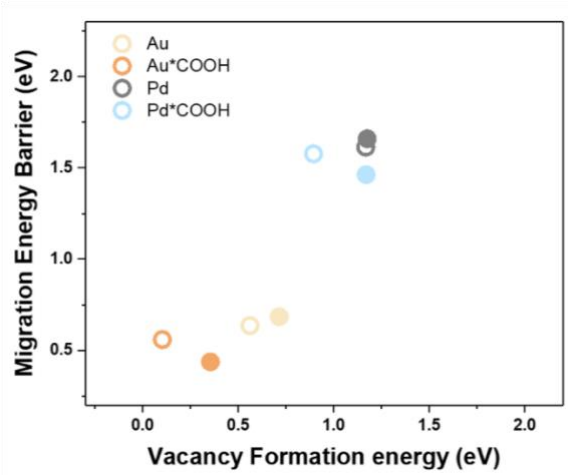

Supplementary Figure 21. Atomic migration energy barrier and atomic vacancy formation energy calculated for (100) facet of Au and Pd with and without surface-bound intermediates *COOH. Hollow and solid circles denote the metal surface with and without the adsorption of potassium ion from the electrolyte, respectively.

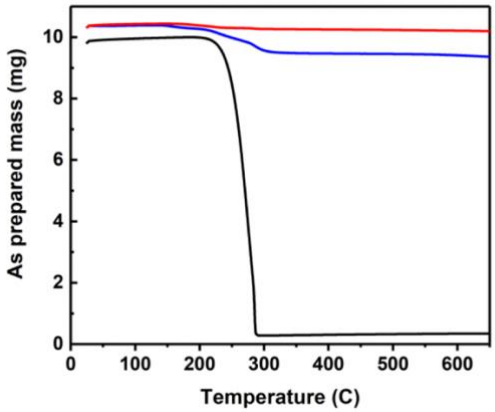

Supplementary Figure 22. Thermogravimetric analysis of cationic surfactant left in the nanoparticle samples on the example of Pd BNPs: as-synthesized Pd BNPs cleaned from excess CTAB with 2 centrifugation cycles in ultrapure water (blue trace) and Pd BNPs dried as a film and subsequently washed with methanol (red trace); CTAB-only TGA trace is shown for reference (black trace).

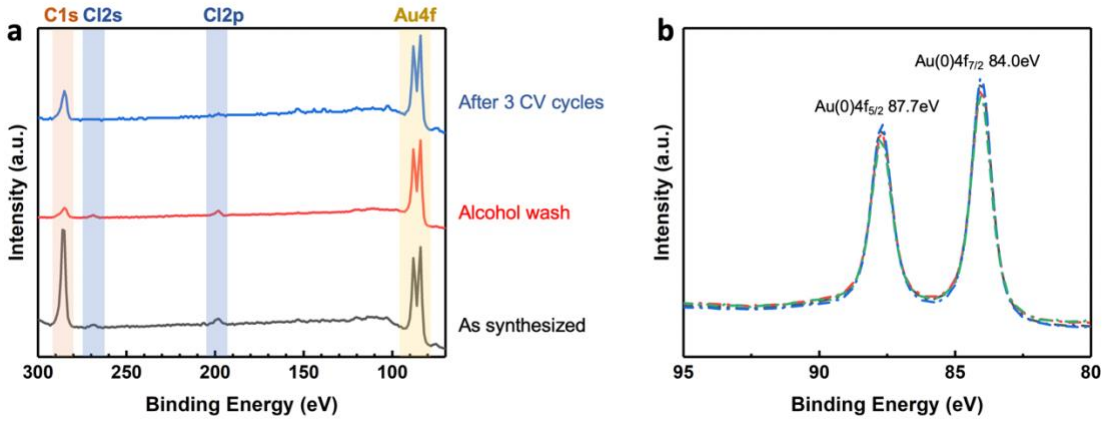

Supplementary Figure 23. Surface analysis of as-synthesised, washed, and electrochemically treated Au CCs. (a) XPS of as-synthesized cetylpyridinium chloride-stabilized nanoparticles (black trace) show the presence of organic ligand stabilizers (C 1s) and chemisorbed chloride ions (Cl 2s and 2p); alcohol wash resulted (red trace) in a significant decrease of [C]:[Au] atomic ratio; after 3 CV cycles at 50mV/s in 0.5M $KHCO_3$ (blue trace), [C]:[Au] atomic ratio doubled compared to that after alcohol wash due to chemisorption of CO_2RR intermediates or bicarbonate ions from the electrolyte. (b) XPS Au 4f spectra show that Au is in metallic state in gold CC nanoparticles as synthesized (black trace), after alcohol wash (red trace), after 3 CV cycles in CO_2-saturated 0.5M $KHCO_3$ from 0 to -1.2V vs RHE (blue trace), and after 5 hours of electrolysis at -0.6V vs RHE (green trace).

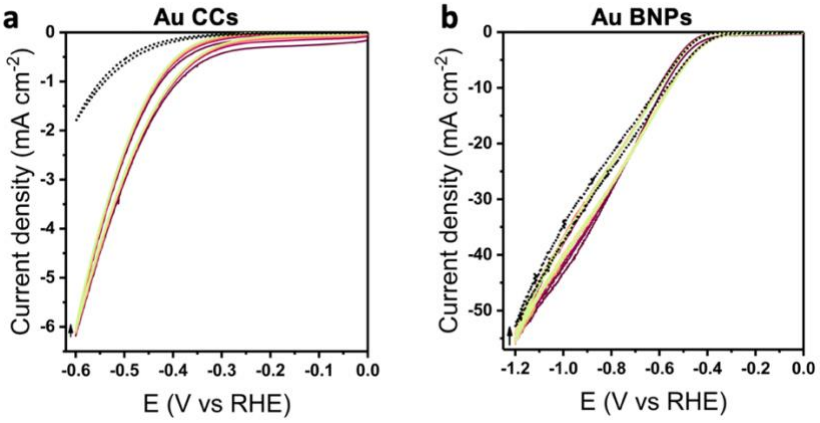

Supplementary Figure 24. Series of 10 CV cycles in CO_2-saturated 0.5M $KHCO_3$ using freshly prepared nanoparticle electrodes (shown in red-yellow color gradient, with the arrow indicating increasing number of cycles) and CV recorded after 5 hours of potentiostatic electrolysis (shown as a black dotted trace) at -0.6V vs RHE for Au CCs (a) and Au BNPs (b).

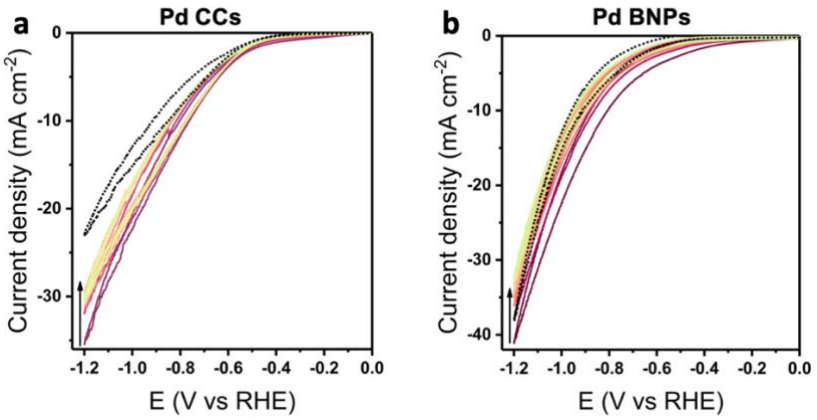

Supplementary Figure 25. Series of 10 CV cycles in CO_2-saturated 0.5M $KHCO_3$ using freshly prepared nanoparticle electrodes (shown in red-yellow color gradient, with the arrow indicating increasing number of cycles) and CV recorded after 5 hours of potentiostatic electrolysis (shown as a black dotted trace) at -1.2V vs RHE for Au CCs (a) and Au BNPs (b).

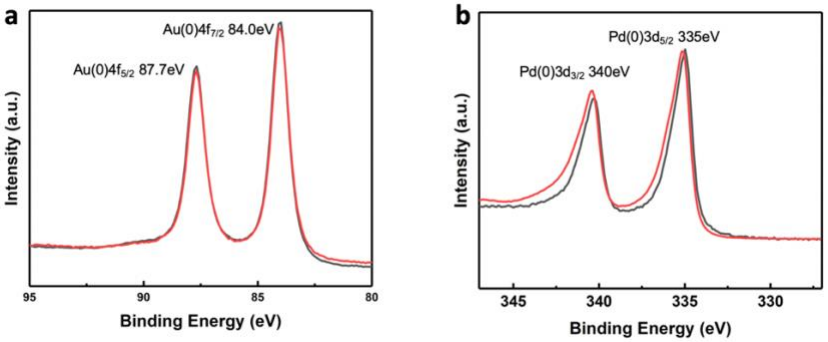

Supplementary Figure 26. XPS surface analysis of nanoparticles after alcohol wash and 3 CV cycles in CO_2-saturated 0.5M $KHCO_3$ from 0 to -1.2V vs RHE. (a) 4f peaks of Au CCs (black trace) and Au BNPs (red trace). (b) 3d peaks of Pd CCs (black trace) and Pd BNPs (red trace).

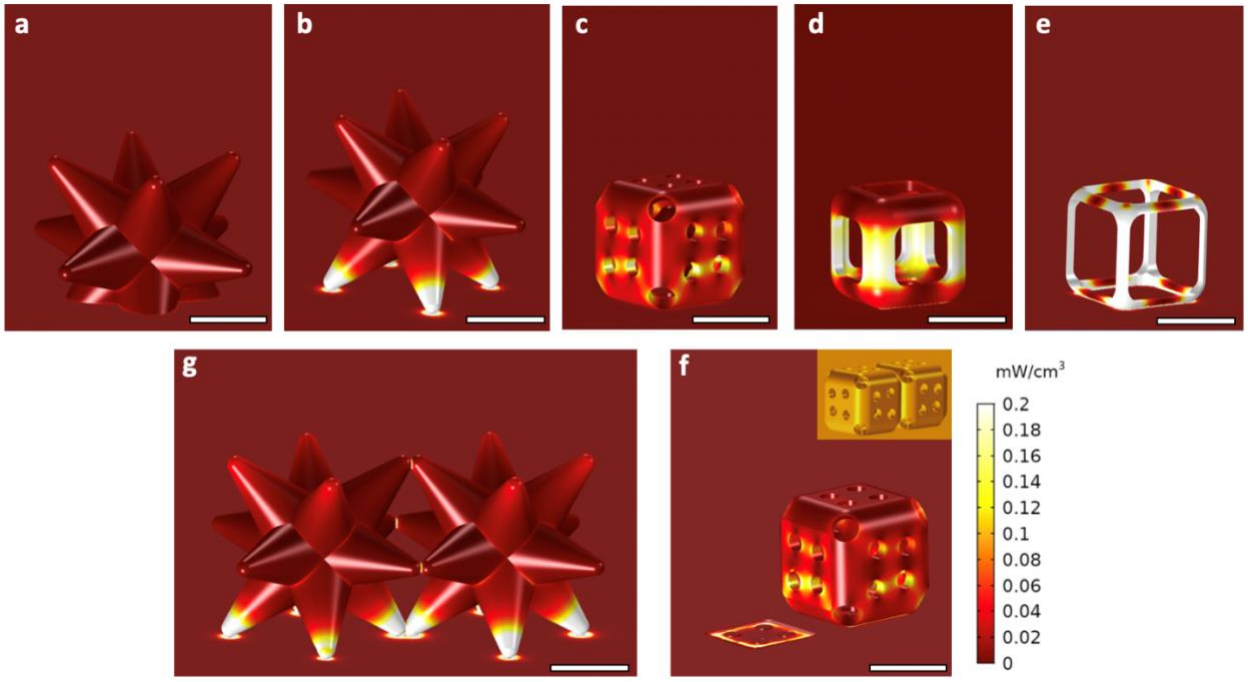

Supplementary Figure 27. Computed power density distribution (shown as colour map) in Au nanostructures of different shapes. The left CC in a dimer in (f) is hidden from view to show the power distribution at the interface between the CC and the substrate, and at the interface between the two CCs; the inset shows the geometry of the dimer. Scale bars are 25 nm.

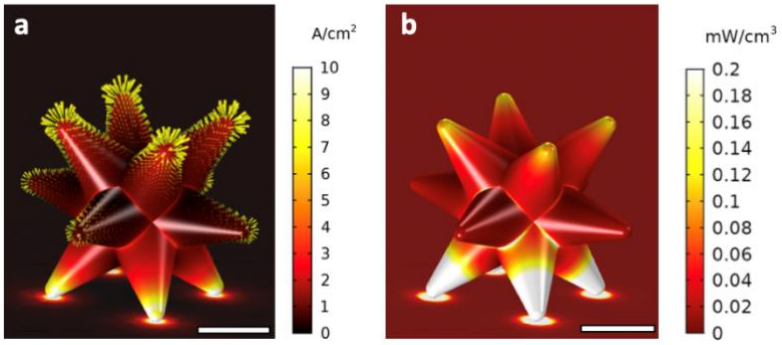

Supplementary Figure 28. Computed current density (a) and power density (b) distributions in Pd BNPs. (a) $J_{electrolyte}$ in are shown as groups of arrows, where the size and direction of each arrow represent the magnitude and direction of current at the spatial position of the arrow; J_{metal} is shown with a colour map. (b) Power density distribution is shown as a colour map. Scale bars are 25 nm.

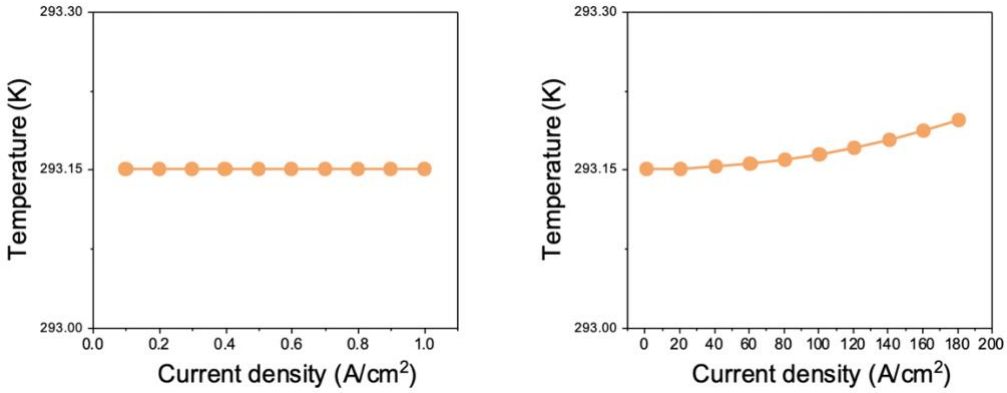

Supplementary Figure 29. The change of averaged temperature of Au BNPs with the average current density with the substrate temperature of 293.15 K as the reference temperature.

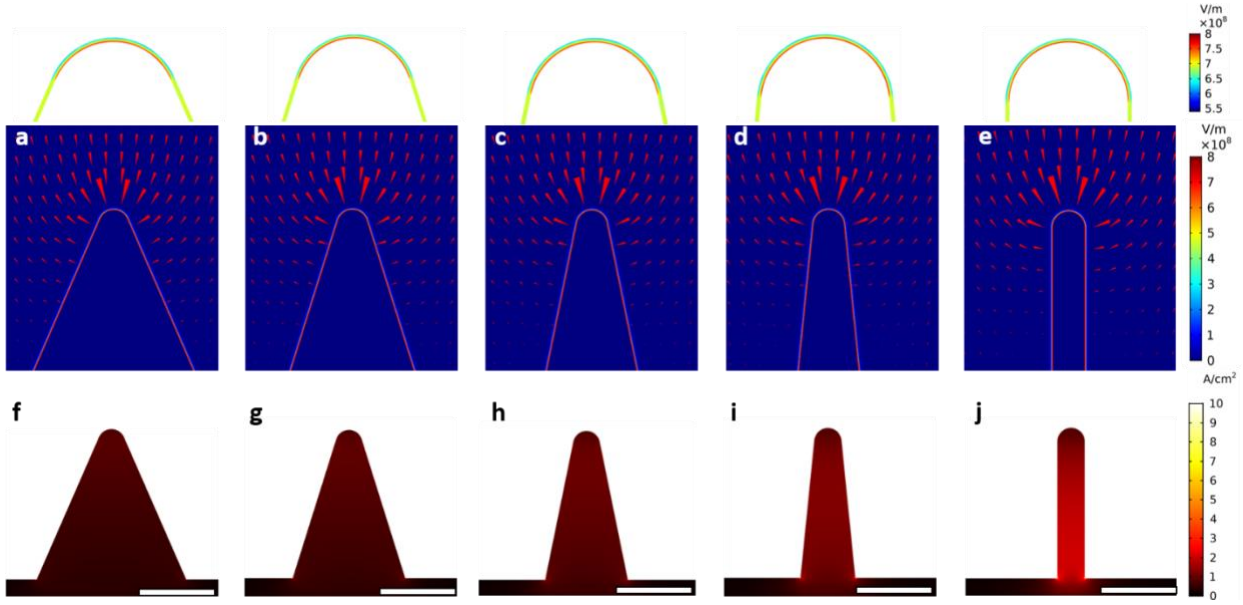

Supplementary Figure 30. Computed E-field and current density distributions (in 2D cross-sections) of extruded Au features with different contact areas with the electrode surface, illustrating the effect of curvature and surface contact. (a-e) E-field intensity at the electrode surface and surrounding electrolyte is shown as a colour map, with the E-field intensity in Stern layer at the apex of the structure is highlighted in the top insets. $J_{electrolyte}$ is shown as groups of arrows, where the size and direction of each arrow represent the magnitude and direction of current at the spatial position of the arrow. (f-j) J_{metal} distribution within the metal structures shown as a colour map. Scale bars are 25 nm.

Supplementary References

1. Klinkova, A. et al. Shape-dependent interactions of palladium nanocrystals with hydrogen. *Small* **12**, 2450-2458 (2016).
2. Yasunaga, H., Natori, A. Electromigration on semiconductor surfaces. *Surf. Sci. Rep.* **15**, 205-280 (1992).
3. Song, T.-B. et al. Nanoscale joule heating and electromigration enhanced ripening of silver nanowire contacts. *ACS Nano* **8**, 2804-2811 (2014).
4. Xia, Y., Xiong, Y., Lim, B. & Skrabalak, S. E. Shape-controlled synthesis of metal nanocrystals: simple chemistry meets complex physics? *Angew. Chem. Int. Ed.* **48**, 60-103 (2009).
5. Khairullina, E. et al. An aligned octahedral core in a nanocage: synthesis, plasmonic, and catalytic properties. *Nanoscale* **11**, 3138–3144 (2019).
6. Choi, S., Moon, Y. & Yoo, H. finely tunable fabrication and catalytic activity of gold multipod nanoparticles. *J. Colloid Interface Sci.* **469**, 269–276 (2016).
7. Klinkova, A., Larin, E. M., Prince, E., Sargent, E. H. & Kumacheva, E. Large-scale synthesis of metal nanocrystals in aqueous suspensions. *Chem. Mater.* **28**, 3196–3202 (2016).
8. Wang, P. et al. Phase and structure engineering of copper tin heterostructures for efficient electrochemical carbon dioxide reduction. *Nat. Commun.* **9**, 1–10 (2018).
9. Zhou, J.-H. et al. Thin-Walled Hollow Au–Cu nanostructures with high efficiency in electrochemical reduction of CO_2 to CO, *Inorg. Chem. Front.* **5**, 1524-1532 (2018).
10. Zhuang, T.-T. et al. Copper nanocavities confine intermediates for efficient electrosynthesis of C3 alcohol fuels from carbon monoxide. *Nature Catal*. **1**, 946-951 (2018).
11. Lee, H.-E. et al. Concave rhombic dodecahedral Au nanocatalyst with multiple high-index facets for CO_2 reduction. *ACS Nano.* **9**, 8384-8393 (2015).
12. Zou, C. et al. Porous copper microspheres for selective production of multicarbon fuels via CO_2 electroreduction. *Small.* **15**, 1902582 (2019).
13. Tan, W. et al. Electrochemical reduction of CO_2 on Hollow Cubic Cu_2O@Au Nanocomposites. *Nanoscale Res. Lett.* **14**, 63 (2019).
14. Liu, S.-Q. et al. Hollow porous Ag spherical catalysts for highly efficient and selective electrocatalytic reduction of CO_2 to CO. *ACS Sustain. Chem. Eng.* **7**, 14443-14450 (2019).
15. Huang, J., Hu, Q., Guo, X., Zeng, Q. & Wang, L. Rethinking $Co(CO_3)_{0.5}(OH)\cdot 0.11H_2O$: a new property for highly selective electrochemical reduction of carbon dioxide to methanol in aqueous solution. *Green Chem.* **20**, 2967-2972 (2018).
16. Zhang, X.-F., Wang, A.-J., Zhang, L., Yuan, J., Li, Z. & Feng, J.-J. Solvothermal synthesis of monodisperse PtCu dodecahedral nanoframes with enhanced catalytic activity and durability for hydrogen evolution reaction, *ACS Appl. Energy Mater.* **1**, 5054-5061 (2018).
17. Wang, Y. et al. Fabrication of bilayer Pd-Pt nanocages with sub-nanometer thin shells for enhanced hydrogen evolution reaction, *Nano Res.* **12**, 2268-2274 (2019).
18. Li, Z. et al. Mesoporous hollow Cu−Ni Alloy nanocage from core−shell Cu@Ni Nanocube for efficient hydrogen evolution reaction. *ACS Catal.* **9**, 5084-5095 (2019).
19. Si, C.-D. et al. Enhanced the hydrogen evolution performance by ruthenium nanoparticles doped into cobalt phosphide nanocages, *ACS Sustainable Chem. Eng.* **7**, 9737-9742 (2019)
20. He, L. et al. Mesoporous nanostructured CoFe−Se−P composite derived from a Prussian blue analogue as a superior electrocatalyst for efficient overall water splitting, *ACS Appl. Energy Mater.* **1**, 3915-3928 (2018).
21. Dai, Z. et al. Hexagonal-phase Cobalt Monophosphosulfide for highly efficient overall water splitting, *ACS Nano* **11**, 11031-11040 (2017).
22. Jiang, Y., Qian, X., Zhu, C., Liu, H. & Hou, L. Nickel cobalt sulfide double-shelled hollow nanospheres as superior bifunctional electrocatalysts for photovoltaics and alkaline hydrogen evolution, *ACS Appl. Mater. Interfaces* **10**, 9379-9389 (2018).
23. Park, S.-K., Kim, J. K. & Kang, Y. C. Metal–organic framework-derived $CoSe_2$/$(NiCo)Se_2$ box-in-box hollow nanocubes with enhanced electrochemical properties for sodium-ion storage and hydrogen evolution, *J. Mater. Chem. A.* **5**, 18823-18830 (2017).

24. Nazemi, M., Panikkanvalappil, S. R. & El-Sayed, M. A. Enhancing the rate of electrochemical nitrogen reduction reaction for ammonia synthesis under ambient conditions using hollow gold nanocages, *Nano Energy* **49**, 316-323 (2018).
25. Nazemi, M. & El-Sayed, M.A. The role of oxidation of silver in bimetallic gold−silver nanocages on electrocatalytic activity of nitrogen reduction reaction, *J. Phys. Chem. C* **123**, 11422-11427 (2019).
26. Ye, W. et al. $Pt_4PdCu_{0.4}$ alloy nanoframes as highly efficient and robust bifunctional electrocatalysts for oxygen reduction reaction and formic acid oxidation, *Nano Energy* **39**, 532-538 (2017).
27. Park, J., Wang, H., Vara, M. & Xia, Y. Platinum cubic nanoframes with enhanced catalytic activity and durability toward oxygen reduction, *ChemSusChem* **9**, 2855-2861 (2016).
28. Chen, C. et al. Highly crystalline multimetallic nanoframes with three-dimensional electrocatalytic surfaces, *Science* **343**, 1339-1343 (2014).
29. Luo, S., Tang, M., Shen, P. K. & Ye, S. Atomic-Scale preparation of octopod nanoframes with high-index facets as highly active and stable catalysts, *Adv. Mater.* **29**, 1601687 (2017).
30. Lyu, L.-M., Kao, Y.-C., Cullen, D. A., Sneed, B. T., Chuang, Y.-C. & Kuo, C.-H. Spiny Rhombic Dodecahedral CuPt Nanoframes with Enhanced Catalytic Performance Synthesized from Cu Nanocube Templates, *Chem. Mater.* **29**, 5681-5692 (2017).
31. Zhu, G., Liu, J., Li, S., Zuo, Y., Li, D. & Han, H. Nickel-ion-oriented fabrication of spiny PtCu Alloy Octahedral Nanoframes with enhanced electrocatalytic performance, *ACS Appl. Energy Mater.* **2**, 2862-2869 (2019).
32. Greenwood, N.N. & Earnshaw, A. *Chemistry of the Elements*, 2nd ed. (Butterworth-Heinemann, 1997).
33. Hamelin, A. Underpotential deposition of lead on single crystal faces of gold: Part I. The influence of crystallographic orientation of the substrate. J. Electroanal. Chem., **165**,167-180 (1984).